Japanese Journal of Applied Physics **57**, 120306 (2018) **RAPID COMMUNICATION**
https://doi.org/10.7567/JJAP.57.120306

Detailed analysis and performance limiting mechanism of Si delta-doped GaAs tunnel diode grown by MBE

Seokjin Kang[1,3], Gun Wu Ju[1], Jung-Wook Min[2], Dong-Seon Lee[1], Yong Tak Lee[1], Hyo Jin Kim[3*], and Kwangwook Park[4,5*]

[1]*School of Electrical Engineering and Computer Science, Gwangju Institute of Science and Technology, Gwangju 61005, Republic of Korea*
[2]*Department of Physics and Photon Science, Gwangju Institute of Science and Technology, Gwangju 61005, Republic of Korea*
[3]*Photonic Energy Research Center, Korea Photonics Technology Institute, Gwangju 61007, Republic of Korea*
[4]*National Renewable Energy Laboratory, Golden, CO 80401, U.S.A.*
[5]*Korea Advanced Nano Fab Center, Suwon, Gyeonggi-do 16229, Republic of Korea*

*E-mail: hjk@kopti.re.kr; kwangwook.park@kanc.re.kr

Received July 10, 2018; accepted October 5, 2018; published online October 30, 2018

High-performance GaAs tunnel diodes (TDs) are fabricated by using Si delta-doping technique. The GaAs TDs exhibited a high peak tunnel-current density of 2,735 A/cm^2 and low specific resistivity of 1.46 × 10^{-4} Ω·cm^2. However, the performance of the GaAs TDs deteriorated once the amount of Si delta doping exceeded a certain limit, which has been rarely reported elsewhere. Detailed analyses and numerical simulations of GaAs TDs with various amounts of Si delta doping prove that Si amphoteric behavior governs the performance limit. GaAs TDs with precisely controlled Si delta doping are suitable for cutting-edge tandem solar cell applications.

Tunnel diodes (TDs), which were invented by Leo Esaki, consist of highly doped (>10^{19} cm^{-3}) PN junctions.[1)] At these junctions, carriers travel through potential barriers while maintaining their original potential energy, which is called the "tunneling effect".[1)] TDs have been used in several applications, such as vertical cavity surface-emitting lasers (VCSELs), light-emitting diodes (LEDs), high electron mobility transistors (HEMTs), and wavelet generators, etc.[2–5)] In particular, TDs have been used in monolithic multi-junction solar cells (MJSCs) as an essential component for connecting sub-cells.[6–9)] By placing the TDs between sub-cells in MJSCs, photo-generated carriers flow throughout serially interconnected sub-cells without being interrupted by potential barriers. The efficiency of the III–V MJSCs has been increased dramatically from 32.6 to 46% over the past two decades.[10,11)] However, the efficiency enhancement gets slower recently even with utilization of many exotic techniques such as direct wafer bonding, bi-facial epitaxy growth, metamorphic growth, and so on.[12–14)] In short, the efficiency of III–V MJSCs was increased by 1.6% only in recent 5 years.[11,15)] In the same period, the efficiency enhancement of perovskite solar cells was 9.5% which is much higher than that of III–V MJSCs.[11,15,16)] It is sure that to compare them directly is not fair; III–V MJSCs pave the way for several decades and research on perovskite solar cell is just started. On the other hand, however, this fact reflects that there are technological limits in enhancing III–V MJSCs efficiency and addresses that it is necessary to find out ways to break through. In this term, improving the performance of TDs would be one of the possible solutions to enhance the efficiency of III–V MJSCs.

TDs for high-efficiency III–V MJSCs must satisfy several requirements; 1) high tunnel current to facilitate the flow of photo-generated carriers, 2) low resistivity to minimize voltage drops at TDs, and 3) small thickness to reduce light absorption by the TDs thus to increase light absorption by the sub-cells. In principle, the requirements for TDs demand high hole and electron concentrations (>10^{19} cm^{-3}) in ultra-thin junctions. However, growing such TDs as-designed is difficult due to practical limits of the dopants.[17–19)] Fortunately, sufficiently high hole concentrations (10^{19}–10^{20} cm^{-3}) with low dopant diffusion across neighboring layers and good surface morphology can be obtained by Be-doped p-GaAs that is grown by the low-temperature molecular beam epitaxy (MBE) technique.[20)] Meanwhile, the highest achievable electron concentrations in Si-doped n-GaAs are only 10^{18}–10^{19} cm^{-3}. This is because Si which is a typical n-type dopant for GaAs grown by MBE is incorporated on As sites (Si_{As}, acceptor) rather than Ga sites (Si_{Ga}, donor) when the bulk doping concentration of Si exceeds 10^{19} cm^{-3} approximately, which is called "Si amphoteric behavior".[19,21)] Te doping in GaAs has been studied as an alternative to obtain high electron concentrations, but this approach is more suitable for metal–organic vapor-pressure epitaxy (MOVPE) than for MBE because of the high vapor pressure and memory effect of Te.[22)]

The delta-doping technique has been examined to obtain high electron concentrations beyond the solubility limit of Si.[23–25)] This technique suppresses the incorporation of Si on As sites (Si_{As}) by supplying Si and As only in absence of Ga during the growth of Si-doped GaAs. Thus, Si amphoteric behavior can be suppressed, so most of Si atoms can be incorporated at Ga sites (Si_{Ga}), producing higher electron concentrations. Indeed, the enhancement of GaAs TD performance by delta doping has been reported elsewhere.[26,27)] DeSalvo et al. reported a delta-doped TD with a tunnel current density of 133 A/cm^2 ($V = 0.1$ V) and specific resistivity of 6×10^{-4} Ω·cm^2 ($V = 0.02$ V), which was superior to TDs without delta doping.[27)] Although delta-doped TDs exhibit excellent performance and potential for further performance improvement, in-depth research and detailed analyses of delta-doped TDs have not yet been reported. In this article, we revisit Si delta-doped GaAs TDs, analyze and discuss the optimization of Si delta doping along with numerical simulations on the device performance.

The samples were grown on a (100) Si-doped n-GaAs substrate by a VG V80H-10K MBE system, which was equipped with a valved cracker effusion cell as the As dimer source. Standard effusion cells were deployed to deliver group-III and dopant elements. Si and Be were used to grow n- and p-type GaAs layers, respectively. Figure 1(a) shows a schematic of the sample structure. Sample growth was initiated by growing Si-doped n-type layers first, followed by Be-doped p-type layers. Prior to sample growth, the substrate was thermally cleaned to remove native oxides at 610 °C for

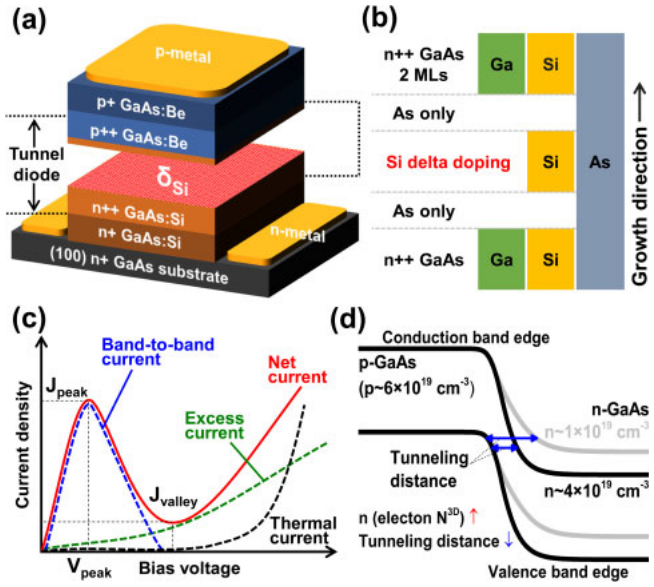

Fig. 1. (Color online) (a) Si delta-doped GaAs TD structure and (b) detailed Si delta-doping sequence in n++GaAs in the tunnel region. (c) Schematic of the current-density curve as a function of the bias voltage. The net tunnel current consists of band-to-band and excess tunnel current. The thermal current is neglected because TDs in MJSCs operate in low bias voltage. (d) Band diagram of a PN junction with two different carrier concentrations.

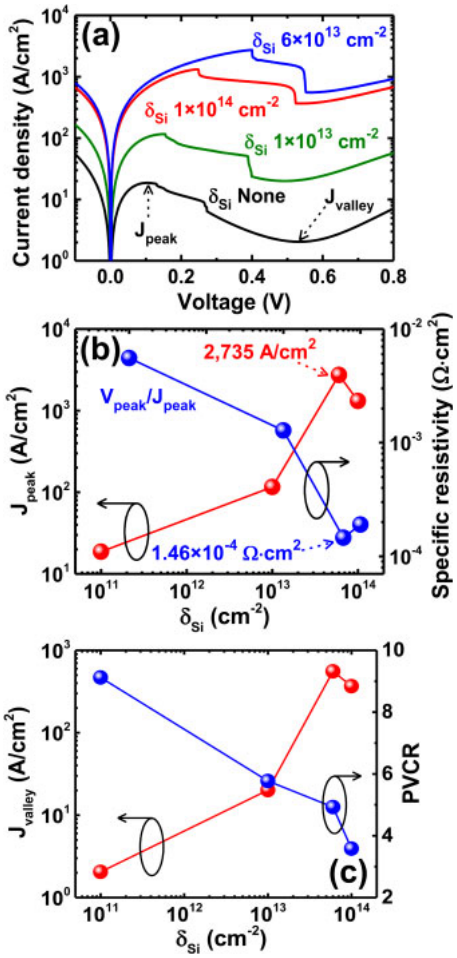

Fig. 2. (Color online) (a) J–V curves GaAs TDs as a function of δ_{Si}. (b) J_{peak} and specific resistivity as a function of δ_{Si}. The upper-bounded J_{peak} and lower-bounded specific resistivity when $\delta_{Si} = 6 \times 10^{13}\,cm^{-2}$ indicate the electron-concentration limit in the n++GaAs layer of the TD. (c) J_{valley} and PVCR as a function of δ_{Si}.

10 min under As overpressure. Then, the substrate surface was covered with a 100-nm-thick n-GaAs buffer layer with a doping concentration of $5 \times 10^{18}\,cm^{-3}$ at 570 °C with V/III = 20. After growing a moderately doped n+GaAs buffer layer, the substrate temperature was lowered to 480 °C to grow 15/15-nm-thick, highly doped p++/n++GaAs layers. The growth temperature was far below the optimum growth temperature of GaAs, but the temperature was known to be suitable to increase the incorporation of Si on donor sites and Be on acceptor sites in GaAs.[19,21)] A n++GaAs layer with a doping concentration of $1 \times 10^{19}\,cm^{-3}$ was grown, followed by a p++GaAs layer with a doping concentration of $6 \times 10^{19}\,cm^{-3}$, thereby completing the TD. Finally, a 100-nm-thick Be-doped p+GaAs contact layer with a carrier concentration of $1 \times 10^{19}\,cm^{-3}$ was grown. Notably, the maximum achievable electron concentration by Si bulk doping in GaAs was around $1 \times 10^{19}\,cm^{-3}$ even at low growth temperatures because of Si amphoteric behavior.[19,21)] To resolve this issue, Si delta doping was applied to obtain higher electron concentration in n++GaAs.

Figure 1(b) shows the detailed growth procedure of Si delta doping in a TD. The location of the Si delta-doping plane was designed to form an abrupt PN doping profile. A two-dimensional Si delta-doping layer was placed two monolayers (MLs) beneath the n++GaAs layer's top. The 2-ML n++GaAs layer on delta-doping layer was intended to prevent possible direct carrier neutralization between the Si delta-doping plane and p++GaAs layer. Also, the location was intended to suppress Si diffusion in GaAs layers by neighboring p++GaAs layer.[28)] The Si supply of the two-dimensional delta-doping concentration (δ_{Si}) was estimated based on the three-dimensional bulk concentration (N^{3D}) and growth rate of Si-doped n-GaAs.[24)] The N^{3D} of electrons and the growth rate of Si-doped n-GaAs was $1 \times 10^{19}\,cm^{-3}$ and 1.02 Å/s, respectively, so the expected δ_{Si} rate was 1.02×10^{11} atoms/(cm^2·s) following δ_{Si} rate = Si N^{3D} × growth rate. In this estimation, we assumed that all Si atoms were incorporated in Ga sites (donor sites). Following this assumption, we also estimated that the reference sample (TD without δ_{Si}) had $\delta_{Si} = 1.02 \times 10^{11}\,cm^{-2}$ in the cross-sectional area. Three different δ_{Si} were chosen for the growth of Si delta-doped TDs, namely, 1×10^{13}, 6×10^{13}, and $1 \times 10^{14}\,cm^{-2}$, which corresponded to 98, 588, and 980 s of Si delta doping duration, respectively. TDs were then fabricated by using a standard semiconductor-fabrication procedure. Au/Ge/Ni/Au and Ti/Pt/Au were used for the ohmic-metal contacts of n-GaAs and p-GaAs, respectively. To define the device, a $50 \times 50\,\mu m^2$ isolated area was formed through wet chemical etching by using an ohmic-metal pad for p-GaAs as an etching mask. To obtain current–voltage curves for the TDs, four-point-probe method was used to minimize the series resistance of the external electrical connections.[2)]

Figures 2(a) shows the current density–voltage (J–V) curves of the GaAs TDs with various δ_{Si}. All the samples showed the characteristic curve of typical TDs.[1)] An Esaki peak (J_{peak}) and negative differential resistivity (NDR) was observed in the J–V curves. Figure 2(b) displays the J_{peak} and specific resistivity (V_{peak}/J_{peak}, where V_{peak} is the voltage at

J_{peak}) as a function of δ_{Si}; these two parameters represent the performance of the TDs. Both of the J_{peak} and specific resistivity were improved in all the delta-doped TDs. The highest J_{peak} (2,735 A/cm^2) and lowest specific resistivity ($1.46 \times 10^{-4}\,\Omega{\cdot}cm^2$) were obtained from a TD with a δ_{Si} of $6 \times 10^{13}\,cm^{-2}$. The estimated voltage drop in the TD was 2.3 μV in MJSCs under 1 sun (current density at 1 sun is ~15 mA/cm^2). Since the open circuit voltage of modern III–V MJSCs is higher than 2.4 V, the efficiency degradation by voltage drop in this TD is negligibly small. In addition, the TD had the maximum capable concentration exceeding 180,000 suns. As far as we know, this result is a record-highest one for an MBE-grown ultra-thin (15 nm/15 nm) GaAs TD. Therefore, it is confirmed that delta-doped TD is beneficial for both non-concentrated and concentrated photovoltaics. The enhancement of J_{peak} was 2 orders of magnitude higher than that of the reference TD. It is the expectable result because Si delta doping elevates the maximum achievable electron concentration in GaAs, thus can increase the tunneling probability.[26,27] Another notable observation is the performance degradation when δ_{Si} exceeded $6 \times 10^{13}\,cm^{-2}$. The maximum dose of δ_{Si} according to previous reports was around $6 \times 10^{13}\,cm^{-2}$; the enhancement limit, which was similar to our results, was not represented and has been rarely reported elsewhere.[27] In fact, Si delta doping cannot completely suppress the amphoteric behavior, so the highest achievable electron concentration of Si delta doping should be limited.[29–32] Since the J_{peak} and specific resistivity are improved with increase of the carrier concentration, we speculate that the enhancement limit was originated from the electron concentration limit of Si delta doping by Si amphoteric behavior.[33–35]

Notably, J_{peak} can be enhanced by both of band-to-band and excess current, as shown in Fig. 1(c). Band-to-band current is the predominant tunnel current that is generated by a way of direct band-to-band tunneling,[1] and excess current is generated from tunneling through energy states within the band gap.[35] Generally, doping is accompanied by defect sites, which have energy states within the band gap. In addition, the number of defect sites tends to increase as a function of the doping concentration. Thus, higher δ_{Si} creates more defect sites and possibly increases excess current and J_{peak}. Despite the expected increase in defect sites with higher δ_{Si}, J_{peak} was decreased when δ_{Si} was higher than 6×10^{13} cm^{-2}, as shown in Fig. 2(c). This observation indicates that the enhancement of band-to-band current was limited by an electron concentration limit of Si delta doping.

Figure 2(c) shows the current density in the valley of the J–V curve (J_{valley}) and the peak-to-valley current ratio (J_{peak}/J_{valley}, PVCR). J_{valley} and the PVCR indicate the degree of defect sites, with the fact that most of the current in the valley consists of excess current with little band-to-band current, as shown in Fig. 1(c).[35] The PVCR was decreased as a function of δ_{Si} without any lower limit, as shown in Fig. 2(c). Thus, Si delta doping increased the amount of defect sites.[36] In contrast to the PVCR having no limit, J_{valley} was increased as a function of δ_{Si} but exhibited an upper limit when $\delta_{Si} = 6 \times 10^{13}\,cm^{-2}$. This behavior is identical to that of J_{peak} as a function of δ_{Si}. Indeed, J_{valley} was affected by both the carrier concentrations of the TD and defect sites in the TD. As discussed in Refs. 33 and 34, the basic principle of enhancing tunnel current involves cutting down the tunneling distance between the junctions. The tunneling distance is decreased with increasing electron concentration in the PN junction's n-GaAs, as shown in Fig. 1(d). This phenomenon also reduces the tunneling distance by way of defect sites and increases both the band-to-band current and excess current. Furthermore, tunnel current is related to the inverse exponential of the tunneling distance. Therefore, the carrier concentration of TDs can significantly affect both band-to-band and excess current. In effect, two different TDs with the same number of defect sites have different excess current if the carrier concentration is not the same. The J_{valley} limit ($\delta_{Si} = 6 \times 10^{13}\,cm^{-2}$) provides the evidence for this hypothesis; the electron concentration limit of Si delta doping by Si amphoteric behavior causes the upper limit of tunnel current in the TDs.

It is also noteworthy that the crystal defects by δ_{Si} or high Si-doped n-GaAs can be generated in atomic scale. Schubert reported that the surface morphology of Si delta-doped n-GaAs shows no degradation such as cross hatch or precipitates.[25] In addition, dislocations were not observed when the thickness of δ_{Si} on GaAs was below 3 MLs, and the thickness of delta-doped layer in our samples is far below the limit thus it is hardly possible to exhibit the dislocations.[37,38] Instead, another thing to consider is point defects in highly doped layer. High concentration of the point defects such as Si_{Ga}–V_{Ga} (Ga vacancy) and Si_{Ga}–Si_{As} was reported when the Si concentration is around $1 \times 10^{19}\,cm^{-3}$.[39] Since these defects form impurity bands inside the bandgap, they can possibly contribute the formation of the excess current.

To clarify the Si amphoteric behavior of Si delta doping, we calculated the J_{peak} of the TDs as a function of δ_{Si} by using computational methods. Prior to the simulation, we assumed that the device structure had zero contact resistance and perfect current spreading over the contact area. A non-local band-to-band tunneling model with a Wentzel–Kramers–Brillouin (WKB) approximation was used to calculate the tunnel current and tunneling probability in the tunnel region.[34,40] In addition, the PVCR of the experimental result was higher than 1 for all the TDs, so band-to-band current should have been the predominant tunnel current in this simulation. Thus, above-mentioned excess current was excluded in the simulation.

In this simulation, doping profiles of actual TDs were used. Doping profiles were obtained by using secondary ion mass spectrometry (SIMS), as shown in Fig. 3(a). The atomic concentrations of both of Si and Be were calibrated by standard Be-doped p-GaAs (hole N^{3D}: ~$10^{18}\,cm^{-3}$) and Si-doped n-GaAs (electron N^{3D}: ~$10^{18}\,cm^{-3}$) samples. Standard samples were confirmed by four-point-probe Hall-effect measurements. The carrier N^{3D} of the standard samples was far below the doping limits, so we assumed that the dopants were all activated in each standard sample and that the measured carrier N^{3D} was similar to the atomic N^{3D} of the dopants.[19] As shown in Fig. 3(a), the Si N^{3D} was increased in the delta-doping plane with increasing δ_{Si}. The highest Si N^{3D} was around $10^{20}\,cm^{-3}$ when δ_{Si} was $1 \times 10^{14}\,cm^{-2}$. The peak Si N^{3D} was increased by 1 order of magnitude, despite the increase in δ_{Si} was 3 orders of magnitude. Instead, the Si N^{3D} distribution widened with increase in δ_{Si}, creating an asymmetric spatial distribution. The wider Si N^{3D} distribution at

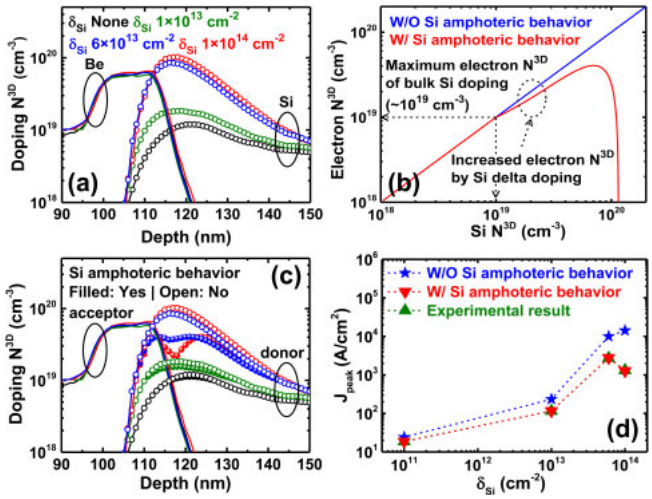

Fig. 3. (Color online) (a) SIMS profiles of TDs with various δ_{Si}. (b) Electron N^{3D}–Si N^{3D} curves with the Si amphoteric behavior. The red curve was calculated with polynomial fitting. (c) Calculated doping profiles that were used in this simulation. The donor valleys with filled circles were the results that were affected by Si amphoteric behavior in (b). (d) Simulation results when using the calculated doping profiles in (c). The blue curve was obtained based on the open-circle dopant profiles in (c) (without Si amphoteric behavior). The red curve was obtained based on the filled-circle dopant profiles in (c) (with Si amphoteric behavior).

high δ_{Si} was caused by the diffusion coefficient increasing as a function of the doping concentration.[29,31,41] The asymmetric spatial Si distribution, which was wider at the bottom and narrower at the top of the TD structure, was caused by the suppression of atomic diffusion from the background doping of Be in p-GaAs.[28]

Si amphoteric behavior was considered to use the doping profiles in this simulation, as shown in Fig. 3(b). This is because the Si profiles of SIMS do not represent the electron concentration but exhibit the atomic concentration instead. The background Si N^{3D} was around $1 \times 10^{19}\,cm^{-3}$ in the TDs' n++GaAs, so we assumed that the Si amphoteric behavior of Si delta doping in n++GaAs appeared when the Si N^{3D} was over $1 \times 10^{19}\,cm^{-3}$. We used the same approach as described in Refs. 30 and 42 by performing a polynomial fitting of the electron N^{3D} to be reduced beyond the 1×10^{19} cm^{-3} threshold, as shown in Fig. 3(b). This curve fitting was repeated until the simulation results showed the same trend as the experimental results. As a result, the fitted Si amphoteric curve exhibited a maximum electron N^{3D} of $4 \times 10^{19}\,cm^{-3}$ at an Si N^{3D} of $7 \times 10^{19}\,cm^{-3}$. Finally, we calculated the donor profiles by using this Si amphoteric curve and redrew the doping profiles, as shown in Fig. 3(c). Since the upper limit of acceptors in Be-doped GaAs is over $10^{20}\,cm^{-3}$, the acceptor profiles were approximated to the Be profiles obtained from SIMS.

The curves with open and filled circles in Fig. 3(c) indicate doping profiles without and with Si amphoteric behavior respectively. A deep donor valley was observed in the donor curve with filled circles because the peak Si N^{3D} (1×10^{20} cm^{-3}) of the TD with a δ_{Si} of $1 \times 10^{14}\,cm^{-2}$ was high enough to be strongly affected by Si amphoteric behavior. On the other hand, the peak Si N^{3D} of the TD with a δ_{Si} of 6×10^{13} cm^{-2} was around $8 \times 10^{19}\,cm^{-3}$, so the Si profile was less affected by Si amphoteric behavior and exhibited a shallow donor valley. Donor valleys from Si delta doping were also found elsewhere.[29]

Table I. J_{peak} (unit: A/cm^2) simulation results of the GaAs TD in Fig. 3(d).

	δ_{Si} (cm^{-2})			
	None	1×10^{13}	6×10^{13}	1×10^{14}
W/O Si amphoteric behavior	24.1	234	10,010	14,202
W/ Si amphoteric behavior	18.5	116	2,778	1,272
Experimental result	18.7	116	2,735	1,315

Figure 3(d) and Table I display the simulation results corresponding to the doping profiles in Fig. 3(c). Without Si amphoteric behavior, the simulation results showed a boundless increase in J_{peak} as a function of δ_{Si}, which completely contrasts how the experimental results indicated an upper limit for J_{peak}. With Si amphoteric behavior, the simulation results matched with the experimental results. Thus, we ascertain that Si delta doping exhibits an electron N^{3D} limit, even though the atomic N^{3D} can be increased monotonically. In fact, the actual maximum electron N^{3D} of Si delta doping should be lower than the calculated one ($4 \times 10^{19}\,cm^{-3}$) because the excess current was excluded in the simulation. However, the simulation results still provide insight into the Si amphoteric behavior of Si delta doping. Finally, we conclude that an optimum δ_{Si} exists for the highest electron N^{3D} and the highest performance of Si delta-doped GaAs TDs.

In summary, Si delta-doped GaAs TDs were characterized, and their performance limitations were analyzed according to the Si amphoteric behavior. The highest J_{peak} (2,735 A/cm^2) was obtained from the device with a δ_{Si} of $6 \times 10^{13}\,cm^{-2}$. Si delta doping significantly improved the performance of the TDs, but the enhancement had an upper limit because of Si amphoteric behavior from the Si delta doping, which was confirmed by the numerical simulation results from the calculated doping profiles with Si amphoteric behavior. Our results can be beneficial for both cutting-edge MJSCs and other device applications that require high-performance tunnel diodes.

Acknowledgement This research was supported by the Technology Development Program to Solve Climate Changes of the National Research Foundation (NRF) funded by the Ministry of Science, ICT(2017M1A2A2048903).

1) L. Esaki, IEEE Trans. Electron Devices **23**, 644 (1976).
2) M. Mehta, D. Feezell, D. A. Buell, A. W. Jackson, L. A. Coldren, and J. E. Bowers, IEEE J. Quantum Electron. **42**, 675 (2006).
3) M. Diagne, Y. He, H. Zhou, E. Makarona, A. V. Nurmikko, J. Han, K. E. Waldrip, J. J. Figiel, T. Takeuchi, and M. Krames, Appl. Phys. Lett. **79**, 3720 (2001).
4) A. Cidronali, G. Collodi, M. Camprini, V. Nair, G. Manes, J. Lewis, and H. Goronkin, IEEE Trans. Microwave Theory Tech. **50**, 2938 (2002).
5) M. Egard, M. Arlelid, E. Lind, G. Astromskas, and L. E. Wernersson, IEEE Microwave Wireless Components Lett. **19**, 386 (2009).
6) I. García, I. Rey-Stolle, and C. Algora, J. Phys. D **45**, 045101 (2012).
7) H. Sugiura, C. Amano, A. Yamamoto, and M. Yamaguchi, Jpn. J. Appl. Phys. **27**, 269 (1988).
8) D. L. Miller, S. W. Zehr, and J. S. Harris, J. Appl. Phys. **53**, 744 (1982).
9) Y. Özen, N. Akın, B. Kınacı, and S. Özçelik, Sol. Energy Mater. Sol. Cells **137**, 1 (2015).
10) M. A. Green, K. Emery, K. Bücher, D. L. King, and S. Igari, Prog. Photovoltaics **5**, 265 (1997).

11) M. A. Green, Y. Hishikawa, E. D. Dunlop, D. H. Levi, J. Hohl-Ebinger, and A. W. Y. Ho-Baillie, Prog. Photovoltaics **26**, 427 (2018).
12) F. Dimroth, T. N. D. Tibbits, M. Niemeyer, F. Predan, P. Beutel, C. Karcher, E. Oliva, G. Siefer, D. Lackner, P. Fuß-Kailuweit, A. W. Bett, R. Krause, C. Drazek, E. Guiot, J. Wasselin, A. Tauzin, and T. Signamarcheix, IEEE J. Photovoltaics **6**, 343 (2016).
13) S. Wojtczuk, P. Chiu, X. Zhang, D. Pulver, C. Harris, and B. Siskavich, AIP Conf. Proc. **1407**, 9 (2011).
14) N. Jain, K. L. Schulte, J. F. Geisz, D. J. Friedman, R. M. France, E. E. Perl, A. G. Norman, H. L. Guthrey, and M. A. Steiner, Appl. Phys. Lett. **112**, 053905 (2018), and references therein.
15) M. A. Green, K. Emery, Y. Hishikawa, W. Warta, and E. D. Dunlop, Prog. Photovoltaics **21**, 827 (2013).
16) D. H. Kim, J. B. Whitaker, Z. Li, M. F. A. M. van Hest, and K. Zhu, Joule **2**, 1437 (2018), and references therein.
17) K. W. Park, S. J. Kang, S. Ravindran, J. W. Min, S. K. Lee, and Y. T. Lee, Semicond. Sci. Technol. **30**, 075008 (2015).
18) K. W. Park, S. J. Kang, S. Ravindran, J. W. Min, S. K. Lee, M. S. Park, and Y. T. Lee, Appl. Phys. Express **8**, 062302 (2015).
19) R. J. Malik, J. Nagle, M. Micovic, T. Harris, R. W. Ryan, and L. C. Hopkins, J. Vac. Sci. Technol. B **10**, 850 (1992).
20) J. L. Lievin and F. Alexandre, Electron. Lett. **21**, 413 (1985).
21) M. Ogawa and T. Baba, Jpn. J. Appl. Phys. **24**, L572 (1985).
22) M. Kamp, G. Mörsch, J. Gräber, and H. Lüth, J. Appl. Phys. **76**, 1974 (1994).
23) K. Ploog, M. Hauser, and A. Fischer, Appl. Phys. A **45**, 233 (1988).
24) E. F. Schubert, J. Vac. Sci. Technol. A **8**, 2980 (1990).
25) E. F. Schubert, J. E. Cunningham, W. T. Tsang, and T. H. Chiu, Appl. Phys. Lett. **49**, 292 (1986).
26) F. W. Ragay, M. R. Leys, and J. H. Wolter, Electron. Lett. **30**, 86 (1994).
27) G. C. DeSalvo, J. Appl. Phys. **74**, 4207 (1993).
28) D. G. Deppe, N. Holonyak, F. A. Kish, and J. E. Baker, Appl. Phys. Lett. **50**, 998 (1987).
29) R. B. Beall, J. B. Clegg, J. Castagne, J. J. Harris, R. Murray, and R. C. Newman, Semicond. Sci. Technol. **4**, 1171 (1989).
30) K. Köhler, P. Ganser, and M. Maier, J. Cryst. Growth **127**, 720 (1993).
31) M. J. Ashwin, M. Fahy, J. J. Harris, R. C. Newman, D. A. Sansom, R. Addinall, D. S. McPhail, and V. K. M. Sharma, J. Appl. Phys. **73**, 633 (1993).
32) L. Hart, M. J. Ashwin, P. F. Fewster, X. Zhang, M. R. Fahy, and R. Newman, Semicond. Sci. Technol. **10**, 32 (1995).
33) J. R. Hauser, Z. Carlin, and S. M. Bedair, Appl. Phys. Lett. **97**, 042111 (2010).
34) M. Hermle, G. Létay, S. P. Philipps, and A. W. Bett, Prog. Photovoltaics **16**, 409 (2008).
35) S. Ahmed, M. R. Melloch, E. S. Harmon, D. T. McInturff, and J. M. Woodall, Appl. Phys. Lett. **71**, 3667 (1997).
36) J. F. Wheeldon, C. E. Valdivia, A. W. Walker, G. Kolhatkar, A. Jaouad, A. Turala, B. Riel, D. Masson, N. Puetz, S. Fafard, R. Arès, V. Aimez, T. J. Hall, and K. Hinzer, Prog. Photovoltaics **19**, 442 (2011).
37) A. Yildiz, S. B. Lisesivdin, H. Altuntas, M. Kasap, and S. Ozcelik, Physica B **404**, 4202 (2009).
38) K. Adomi, S. Strite, H. Morkoç, Y. Nakamura, and N. Otsuka, J. Appl. Phys. **69**, 220 (1991).
39) L. Pavesi, N. H. Ky, J. D. Ganière, F. K. Reinhart, N. Baba-Ali, I. Harrison, B. Tuck, and M. Henini, J. Appl. Phys. **71**, 2225 (1992).
40) M. Baudrit and C. Algora, IEEE Trans. Electron Devices **57**, 2564 (2010).
41) J. J. Harris, R. B. Beall, J. B. Clegg, C. T. Foxon, S. J. Battersby, D. E. Lacklison, G. Duggan, and C. M. Hellon, J. Cryst. Growth **95**, 257 (1989).
42) L. Däweritz, H. Kostial, R. Hey, M. Ramsteiner, J. Wagner, M. Maier, J. Behrend, and M. Höricke, J. Cryst. Growth **150**, 214 (1995).